Received: 6 February 2021 | Accepted: 15 June 2021

DOI: 10.1111/jmi.13040

Journal of Microscopy RMS

ORIGINAL ARTICLE

Three-dimensional transfer function of optical microscopes in reflection mode

Peter Lehmann | **Tobias Pahl**

Measurement Technology Group, Department of Electrical Engineering and Computer Science, University of Kassel, Germany

Correspondence
Peter Lehmann, Department of Electrical Engineering and Computer Science, University of Kassel, 34109 Kassel, Germany.
Email: p.lehmann@uni-kassel.de

Funding information
Deutsche Forschungsgemeinschaft, Grant/Award Numbers: LE 992 14-1, LE 992 16-1

Abstract

Three-dimensional (3D) transfer functions build the basis for a comprehensive characterization of optical imaging systems in the spatial frequency domain. Utilizing the projection-slice theorem, the 2D modulation transfer function of an incoherent imaging system can be derived from a 3D transfer function by integration with respect to the axial spatial frequency. For a diffraction limited microscope with homogeneous incoherent pupil illumination, the modulation transfer function equals the 2D autocorrelation function of a circular disc. However, until now to the best of our knowledge no 3D transfer function has been published, which exactly leads to the 2D modulation transfer function of a diffraction limited microscope in reflection mode. In this article, we derive a formula, which after integration with respect to the axial spatial frequency coordinate perfectly fits to the diffraction limited 2D modulation transfer function. The inverse three-dimensional Fourier transform of the 3D transfer function results in a complex-valued 3D point spread function, from which the depth of field, the lateral resolution and, in addition, the corresponding 3D point spread function of both, a conventional and an interference microscope, can be obtained.

KEYWORDS

3D point spread function, 3D spatial frequency characterization, microscopy, reflection mode, transfer function

1 | INTRODUCTION

About 150 years ago, Ernst Abbe demonstrated that the lateral resolution of optical microscopes is limited even if no aberrations introduced by manufacturing tolerances and maladjustment of optical components occur.[1] Abbe considered a grating of certain period as measuring object and found that the minimum grating period that can be resolved in reflection mode equals $\lambda/(2\,\mathrm{NA})$, where λ is the wavelength of light and NA the numerical aperture of the microscope objective lens. A different approach followed by Lord Rayleigh, which assumes a point light source or scatterer in the object plane and calculates the corresponding intensity distribution in the image plane, results in the so-called point spread function (PSF).[2] For diffraction limited incoherent imaging systems, the PSF equals the well-known Airy disc function. In this context, the lateral resolution limit according to the Rayleigh criterion leads to the minimum separation of two point light sources or scatterers in the object plane, which can be resolved by the

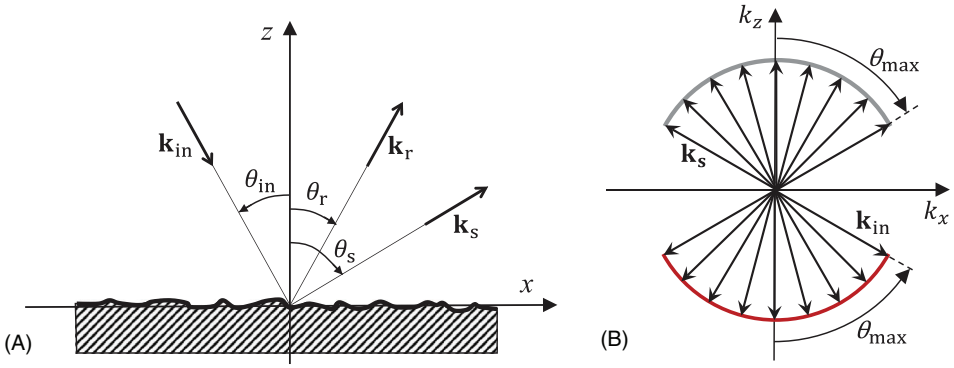

FIGURE 1 Scattering geometry (A) and spherical caps of incident and scattered light (B)

microscope. The Fourier transform of the Airy disc function corresponds to the autocorrelation function of two circular apertures in the spatial frequency domain leading to the well-known expression for the modulation transfer function (MTF) of a diffraction limited system.[3,4] This approach assumes that the objective's pupil is uniformly illuminated obeying the sine condition.[5] However, in contrast to the paraxial approximation it is not limited to small apertures. More recently, the transfer characteristics of microscopes are analysed by 3D transfer functions (3D TFs). These go back to the work of McCutchen, who adapted the Ewald sphere approach and introduced the concept of 3D Fourier transform in context with the diffraction pattern of a single point source.[6] However, these 3D TFs are different for transmission- and reflection-type microscopes.[7–13]) The concept of 3D TFs in context with light microscopy in reflection mode follows from Figure 1. Figure 1(A) shows a single wave vector $\mathbf{k}_{in}$ of an incident plane wave illuminating an object located in the xy-plane under the incidence angle θ_{in}. If the object's surface is flat, the reflected wave is characterized by the wave vector $\mathbf{k}_r$ and the angle θ_r of reflection. If the object's surface consists of single point scatterers the incident plane wave will be scattered, resulting in a scattered light field, which can be described by numerous plane waves, each characterized by a scattered wave vector $\mathbf{k}_s$ and a scattering angle θ_s. In a microscope of given NA and full pupil illumination, there are numerous plane waves incident under different angles up to the angle $\theta_{max} = \arcsin(NA)$ as it is shown in Figure 1(B). For each of these incident waves, the scattered light field can be described by a set of plane waves given by wave vectors $\mathbf{k}_s$. Note that for simplicity the schematics in Figure 1 are cross sections related to the xz- and $k_x\,k_z$-plane, respectively. Further note that the situation is different for a microscope in transmission mode where the z-components of the wave vectors of incident and scattered waves will have the same sign.[10,12,13]

The maximum angle of the scattered waves contributing to the microscope image is again given by θ_{max}. According to Figure 1(B), the vectors of all incident and all scattered waves contributing to the microscope image end on spherical caps. This leads to the construction of an Ewald or McCutchen sphere,[6,7,14] where each end point of a vector $\mathbf{k}_{in}$ is connected to an end point of a vector $\mathbf{k}_s$ resulting in $\mathbf{q} = \mathbf{k}_s - \mathbf{k}_{in}$. The $\mathbf{q}$-space then represents the 3D spatial frequency domain. This concept directly leads to the calculation of the 3D TF by correlating the spherical caps according to Figure 1(B). However, for each $\mathbf{q}$-value, where the correlation integral is different from zero, the pupil functions for the incident and scattered light need to be considered.

According to the projection-slice-theorem,[15] a 2D MTF depending only on the lateral spatial frequency can be obtained by integrating the 3D TF along the vertical spatial frequency axis, that is the optical axis of the microscope. Several approaches to obtain the 3D TF for a bright-field reflection microscope with spatially incoherent illumination have been published. In this context, it should be noted that the 3D TF of a confocal microscope (CM) is known as the coherent 3D TF due to the spatially coherent illumination in the CM. However, the coherent 3D TF of a CM is closely related to the incoherent 3D TF of a conventional reflection microscope.[16] Because of the coherent imaging process, the coherent TF refers to the amplitude (electric field), whereas the incoherent TF is multiplied by the intensity in the spatial frequency domain.[16] Therefore, the coherent 3D TFs introduced by Sheppard et al. in the 1990s[12,17,18] for CMs apply to conventional incoherent bright-field microscopes, if they are related to the intensity instead of the amplitude. Sheppard et al.[17] derive an analytical expression, which holds under the paraxial approximation and results in unity value over nearly the complete range, where the 3D TF differs from zero in the spatial frequency domain. They further show that under this approximation the MTF results in the well-known formula for diffraction limited systems introduced by Hopkins.[3] Another approach by Sheppard et al.[12] considers systems of high numerical aperture and calculates the

autoconvolution of two spherical caps of infinitesimal thickness proportional to the infinitesimal wavelength range $d\lambda$ as their volume of overlap. This integral method leads to elliptic integrals and 3D TFs, which after integration along the axial spatial frequency coordinate differ from the diffraction limited MTF. A further approach based on the Kirchhoff approximation and Fourier optics, which also takes high aperture systems into account, results in a different 3D TF, which is valid for rough surface imaging.[18] The result again leads to an elliptic integral and the corresponding MTF shows much higher values compared to the diffraction limited MTF known from incoherent imaging. More recently, a 3D TF of a focus variation microscope in reflection mode has been derived by correlating two identical spherical caps.[19] This result is totally different from those obtained by the group of Sheppard et al. for microscopes operated in reflection mode.[12,17,18] Nevertheless, focus variation microscopy utilizes the depth discrimination of single point scatterers by spatially resolved analysis of a through focus image stack. This principle requires some intensity modulation in the recorded images and thus it does not work if the object under investigation is a perfect mirror.

The knowledge of the 3D TF of an incoherent microscopic imaging system is crucial for the calculation of the 3D TF of an interference microscope, since the object intensity in most interference microscopes results from an incoherent imaging process of the object's surface.[20] This even holds for a Mirau-type interference microscope if the obscuration by the reference mirror is neglected. Thus, the incoherent 3D TF builds the basis for the calculation of the TF of an interference microscope, too. The reference intensity of an interference microscope in the spatial frequency domain corresponds to the on-axis spatial frequency distribution belonging to specular reflection, that is there are no transverse spatial frequency components different from zero. Hence, for a certain angle of incidence the square root of the reference intensity can be multiplied by the square root of the image intensities in the spatial frequency domain, finally resulting in the 3D TF of the interference microscope.[20] As a concequence, the 3D TF of a bright-field microscope derived for constant pupil illumination equals the 3D TF of an interference microscope. The theoretical 3D TF was recently used in coherence scanning interferometry (CSI) in order to correct 3D transfer and point spread characteristics,[21,22] to analyse defocus effects[23] and to compensate for lens aberration.[24] Furthermore, modelling based on the 3D spatial frequency representation explains that the axial spatial frequency, at which CSI signals are analysed, affects the lateral resolution achieved in CSI measurements.[20,25,26] In this context, it should be noticed that the 3D intensity TF cannot be observed directly as a bandwidth limitation in a conventional microscope. This is a consequence of the fact that microscopic imaging is based on intensities, whereas the transfer characteristics are determined through amplitude and phase modulated signals, which only appear in interferometric systems such as CSI or holographic microscopy.

In the following section, we will introduce a differential approach to calculate a mostly analytical 3D TF for an incoherent imaging microscope. We use the term "incoherent' here, since we assume Kohler illumination and superimpose the intensities for different angles of incidence instead of the electric fields. Although our major intention is to analyse systems of high NA, reducing the NA will result in a partially coherent system because of the limited number of incident plane waves contributing to the imaging process. For such incoherent and partially coherent systems, we show that the corresponding 2D MTF obtained by use of the projection slice theorem[15] perfectly agrees with the well-known MTF of an aplanatic imaging system obeying the sine condition. Therefore, the resulting 3D TF turns out to be quite useful for a comprehensive analysis of both, optical microscopes working in reflection mode as well as interference microscopes used for 3D surface profilometry.

2 | DERIVATION OF THE 3D TF

The coordinates $\mathbf{m} = (m, n, s) = \mathbf{q}/k_0 = (\mathbf{k}_s - \mathbf{k}_{in})/k_0$ we use in the following agree with those introduced by Sheppard et al.[18] where m and n represent the two transverse coordinates and the axial component is given by s. All three components are normalized with respect to the wavenumber $k_0 = 2\pi/\lambda$, such that both, the wave vectors of the incident and the scattered light, end on spherical caps of unity radius. Note that under this assumption the side view of the resulting Ewald limiting sphere representing the cut-off in the spatial frequency domain due to the limited NA of an objective lens equals a portion of a sphere of radius 2, which is cut by a plane.[7,11,17]

Our approach to calculate the 3D TF is closely related to the calculation of the 2D MTF as the overlapping area of two intersecting circular apertures.[4] Since both, the 2D MTF as well as the 3D TF show rotational symmetry the coordinate $l = \sqrt{m^2 + n^2}$ represents the distance from the axis of symmetry. The general physical situation is explained with respect to Figures 2(A) and 3(A). Both, the incident and the scattered wave vectors form a spherical cap. The lateral extension of these caps is limited by the NA of the objective lens. The caps are inverted with respect to each other as shown in Figure 2(A) because of the different propagation direction of the incident and scattered waves with respect to the vertical axis, which equals the optical axis of the system (see Figure 1). The lateral shift l of the two caps represents the lateral spatial frequency, that is the spatial frequency in the image plane that

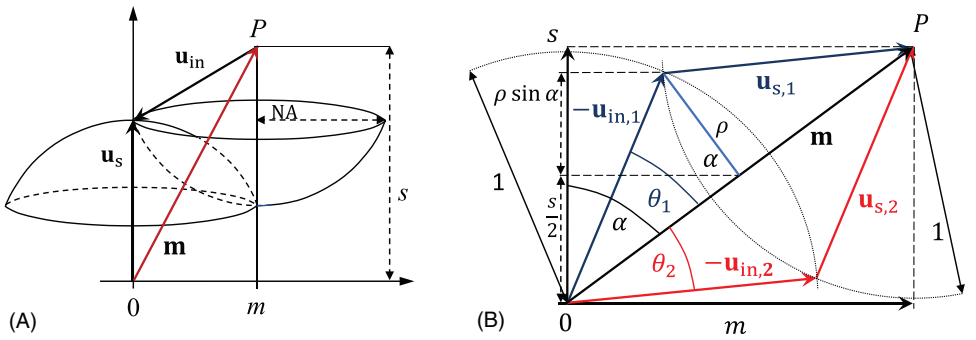

FIGURE 2 Geometry for the derivation of the 3D TF: (A) Two spherical caps corresponding to unity wave vectors of incident waves $\mathbf{u}_{in}$ and scattered waves $\mathbf{u}_s$ are correlated. The point P is defined by vector $\mathbf{m}$ with coordinates m and s in the spatial frequency domain representing the shift of the centres of the two unit spheres; (B) The circle of intersection of the two unit spheres is characterized by the radius ρ and the tilt angle α. The vectors $-\mathbf{u}_{in,1}$, $-\mathbf{u}_{in,2}$, $\mathbf{u}_{s,1}$ and $\mathbf{u}_{s,2}$ corresponding to point P are located in the plane of incidence (ms-plane)

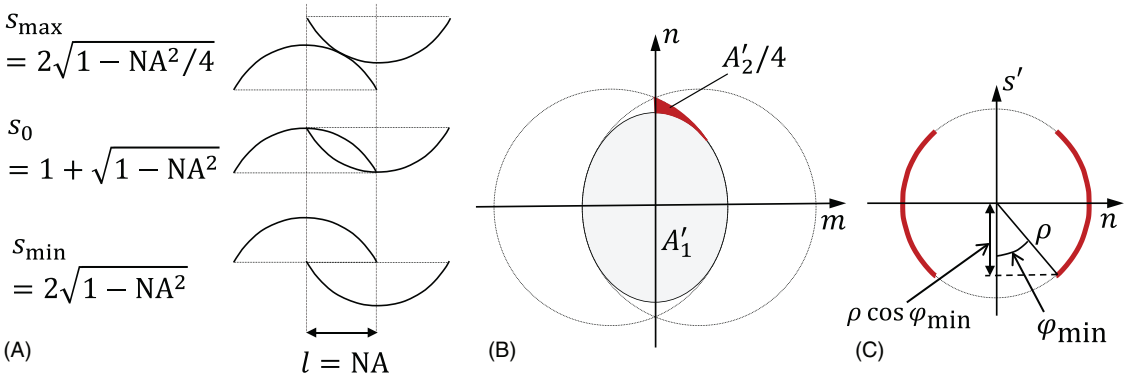

FIGURE 3 Geometry for the derivation of the 3D TF: (A) Spherical caps (side view) for three different height positions s_{max}, s_0, s_{min} and constant lateral shift $l = NA$; (B) Top view representing the area A_1' for height shifts between s_0 and s_{max} as well as area A_2' for height shifts between s_{min} and s_0; (C) Representation of the geometry leading to area A_2' by integration

is limited by 2 NA. The vertical shift represents the axial spatial frequency. Contributions of the spatial frequency components to the imaging process can be expected as long as the two caps according to Figure 2(A) overlap. For a given lateral shift l, the 3D TF solely depends on the vertical shift s as Figure 3(A) demonstrates for $l = NA$. Hence, integration along the s-axis must result in an area that equals the intersection area of two laterally shifted circular apertures, which is represented by the top view in Figure 3(B). In the general case, this area consists of two contributions, area A_1' and area A_2'. Area A_1' results if we integrate from $s_0 = \sqrt{1 - NA^2} + \sqrt{1 - (l - NA)^2}$ to $s_{max} = 2\sqrt{1 - l^2/4}$. Under this assumption, the lines of intersection of the two spherical caps are full circles tilted by the angle α according to Figure 2(B), such that the area A_1' resulting from integration is an ellipse as it is shown in Figure 3(B). In contrast, area A_2' is attributed to the range $s_{min} = 2\sqrt{1 - NA^2}$ (see Figure 3A) to $s_0 = \sqrt{1 - NA^2} + \sqrt{1 - (l - NA)^2}$, where according to Figure 3(C) the lines of intersection of the two spherical caps are subdivided into four parts of equal length. After integration, the sum of these four subareas $A_2'/4$ builds the difference between the intersecting area of the two circles and the ellipse A_1'.

According to Figure 2(B) area A_1 is given by a circle of radius $\rho = \sin\theta_1$. In the ms-plane, the points of intersection of circles of radius 1 centred around the origin and point P are the end points of the two unity vectors $-\mathbf{u}_{in,1}$ and $-\mathbf{u}_{in,2}$ and the starting points of the unity vectors $\mathbf{u}_{s,1}$ and $\mathbf{u}_{s,2}$. These vectors demonstrate that each point P of the TF can be reached by two different ray paths in the ms-plane as described by Quartel and Sheppard.[9] Due to the symmetry of the configuration, the values of the angles θ_1 and θ_2 are the same and can be obtained by

$$\theta_{1,2} = \arccos(|\mathbf{m}|/2), \tag{1}$$

where $|\mathbf{m}| = \sqrt{m^2 + n^2 + s^2} = \sqrt{l^2 + s^2}$. Furthermore, the angle α is given by

$$\alpha = \arccos(s/|\mathbf{m}|). \tag{2}$$

As the area A_1 is tilted by the angle α with respect to the vertical mn-plane the area seen in the top view equals

$$A_1'(s) = A_1 \cos\alpha = \pi \sin^2\theta_1 \cos\alpha = \pi\left(\frac{s}{|\mathbf{m}|} - \frac{s\,|\mathbf{m}|}{4}\right), \tag{3}$$

where

$$\cos\theta_1 = \frac{|\mathbf{m}|}{2} = \frac{\sqrt{l^2+s^2}}{2} \tag{4}$$

and

$$\cos\alpha = \frac{s}{\sqrt{l^2+s^2}}. \tag{5}$$

The area A_1' represents a part of the MTF value for a certain lateral shift l. Since the MTF values follow from integration with respect to the s coordinate we are interested in the derivative

$$\frac{dA_1'(s)}{ds} = \frac{\pi}{|\mathbf{m}|}\left(1 - \frac{s^2}{|\mathbf{m}|^2}\right) - \frac{\pi}{4}|\mathbf{m}|\left(1 + \frac{s^2}{|\mathbf{m}|^2}\right) \tag{6}$$

in order to construct the 3D TF. Hence, the integration of $dA_1'(s)/ds$ from $s_0 = \sqrt{1-\mathrm{NA}^2} + \sqrt{1-(l-\mathrm{NA})^2}$ to $s_{\max} = 2\sqrt{1-l^2/4}$ results in the elliptical area A_1' shown in Figure 3(B).

For $l = 0$, the derivation is linearly related to the coordinate s:

$$\left.\frac{dA_1'(s)}{ds}\right|_{l=0} = \left.\frac{dA_1'(s)}{ds}\right|_{|\mathbf{m}|=s} = -\frac{\pi}{2}s, \tag{7}$$

where the negative sign agrees with the fact that the circle of the largest radius is assigned to the smallest s-value. Note that $l = 0$ corresponds to specularly reflected waves.[8,20] The second contribution to the TF comes from the area A_2', which can be seen again as the projection of a tilted area A_2 consisting of segments of a circle according to Figure 3(C) into the mn-plane. This contribution originates from waves with wave vectors that leave the plane of incidence (ms-plane) according to Figure 2(B). Rays belonging to this region are called skew rays.[8] The area A_2 results from the following integration with respect to the coordinates ρ ans φ (see Figure 3C):

$$A_2 = -4\int_{\rho_{\min}}^{\rho_{\max}}\int_{\varphi_{\min}(\rho)}^{\pi/2} \rho\, d\varphi\, d\rho$$

$$= -4\int_{\rho_{\min}}^{\rho_{\max}}\left(\frac{\pi}{2} - \varphi_{\min}(\rho)\right)\rho\, d\rho, \tag{8}$$

$$\Rightarrow A_2' = A_2\cos\alpha$$

$$= -4\cos\alpha\int_{\rho_{\min}}^{\rho_{\max}}\left(\frac{\pi}{2} - \varphi_{\min}(\rho)\right)\rho\, d\rho, \tag{9}$$

where

$$\rho_{\min} = \sqrt{1 - \frac{l^2+s_0^2}{4}}, \quad \rho_{\max} = \sqrt{1 - \frac{l^2+s_{\min}^2}{4}}.$$

The lower limit $\varphi_{\min}(\rho)$ follows from the equation

$$\rho\cos\varphi_{\min}\sin\alpha = \frac{s}{2} - \sqrt{1-\mathrm{NA}^2} = \frac{s-s_{\min}}{2}, \tag{10}$$

which can be obtained from Figures 2 and 3(C) considering that the minimum shift in s-direction is $s_{\min}$. For $s < s_{\min}$, the spherical caps will no longer overlap. The coordinate s' in Figure 3(C) is tilted by the angle α in the ms-plane such that $s' = m\cos\alpha + s\sin\alpha$. Hence, the vertical component of ρ equals $\rho\cos\varphi_{\min}\sin\alpha$. The derivation of A_2' with respect to s results in:

$$\frac{dA_2'(s)}{ds} = \frac{dA_2(s)}{ds}\cos\alpha + A_2(s)\frac{d\cos\alpha}{ds}. \tag{11}$$

Since

$$\rho = \sin\theta_1 = \sqrt{1-|\mathbf{m}|^2/4}$$

$$\Rightarrow \rho\, d\rho = \rho\frac{d\rho}{ds}ds = -\frac{s}{4}ds \tag{12}$$

with Equations (5), (8), (10) and (12) the first term on the right-hand side of Equation (11) can be written as

$$\frac{dA_2(s)}{ds}\cos\alpha = \left(\frac{\pi}{2} - \arccos\left(\frac{|\mathbf{m}|\,(s-s_{\min})}{l\sqrt{4-|\mathbf{m}|^2}}\right)\right)\frac{s^2}{|\mathbf{m}|}. \tag{13}$$

The second term on the right-hand side of Equation (11) equals

$$A_2(s)\frac{d\cos\alpha}{ds} = A_2(s)\frac{1}{|\mathbf{m}|}\left(1 - \frac{s^2}{|\mathbf{m}|^2}\right). \tag{14}$$

Using Equation (13) and considering that $\cos\alpha = s/|\mathbf{m}|$ for the area $A_2(s)$, the expression

$$A_2(s) = -\int_{s_{\min}}^{s}\frac{dA_2(s')}{ds'}ds'$$

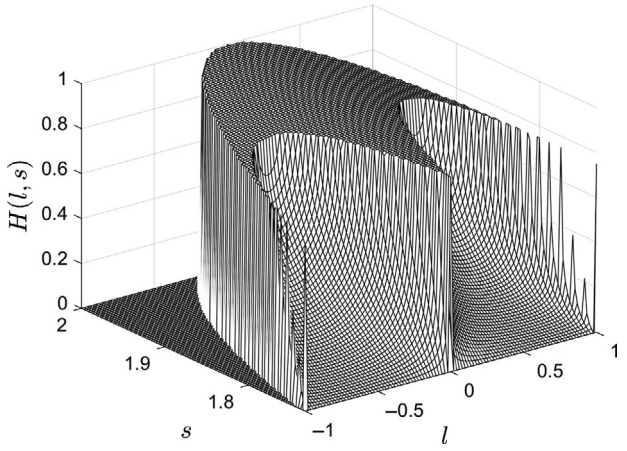

FIGURE 4 3D TF of a microscope in reflection mode assuming NA = 0.5 (the complete 3D TF is rotational symmetric about the s-axis)

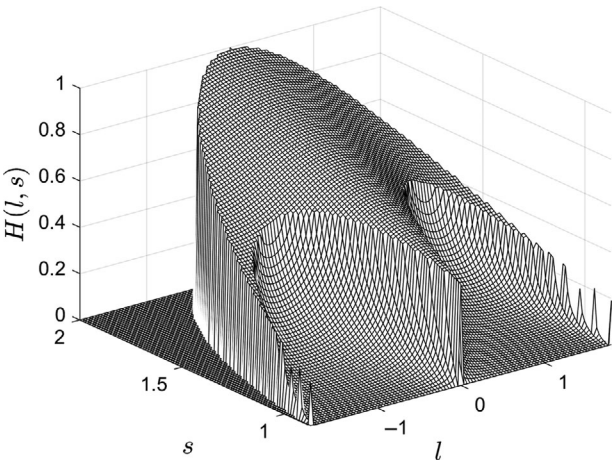

FIGURE 5 3D TF of a microscope in reflection mode assuming NA = 0.9 (the complete 3D TF is rotational symmetric about the s-axis)

$$= -\frac{\pi}{4}\left(s^2 - s_{\min}^2\right) - \int_{s_{\min}}^{s} \arccos\left(\frac{\sqrt{l^2 + s'^2}\,\left(s' - s_{\min}\right)}{l\,\sqrt{4 - \left(l^2 + s'^2\right)}}\right) s'\,ds' \tag{15}$$

can be obtained.

Finally, the 3D TF $H(l, s)$ results in:

$$\begin{aligned} H(l,s) &= \frac{dA_1'(s)}{ds} \quad \text{for} \quad s_0 \le s \le s_{\max}, \\ H(l,s) &= \frac{dA_2'(s)}{ds} \quad \text{for} \quad s_{\min} \le s < s_0, \\ H(l,s) &= 0 \qquad\qquad \text{elsewhere}, \end{aligned} \tag{16}$$

where $dA_1'(s)/ds$ and $dA_2'(s)/ds$ are given by Equations (6), (11), (13) and (14). In the following, $H(l, s)$ is normalized to a maximum value of $H(l = 0, s = 2) = 1$. For the computation of the 3D TFs in the following section, the contribution of the integral according to Equation (15) is calculated numerically by a rectangular approximation and shown to be rather low.

3 | RESULTS

Figures 4 and 5 show examples of the monochromatic 3D TF $H(l, s)$ according to Equation (16) for numerical apertures of 0.5 and 0.9, respectively. Figures 6 and 7 show the contribution according to Equation (13) and the result of Equation (14) including the numerical integration according to Equation (15) for both numerical apertures. For both NA values these results point out that Equation (14) represents only a small portion of the TF compared to the contribution according to Equation (13). Note that Equation

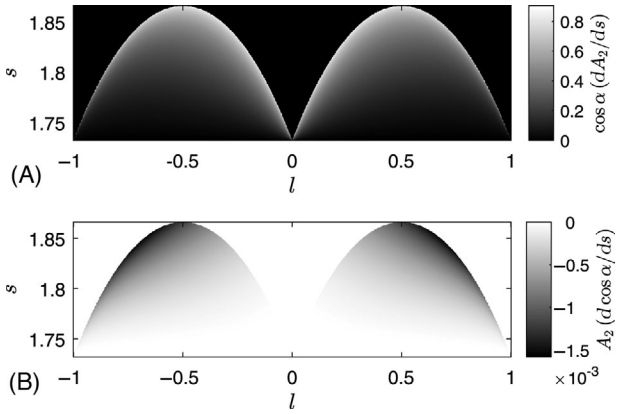

FIGURE 6 Contributions according to Equation (13) (A) and Equation (14) (B) to the 3D TF assuming NA = 0.5. Note that the contribution according to (A) extends from 0 to 0.88, whereas the results shown in (B) range from −0.0016 to 0

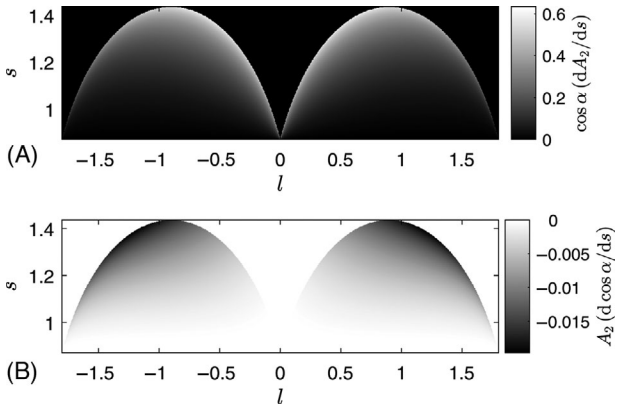

FIGURE 7 Contributions according to Equation (13) (A) and Equation (14) (B) to the 3D TF assuming NA = 0.9. Note that the contribution according to (A) extends from 0 to 0.61, whereas the results shown in (B) range from −0.02 to 0

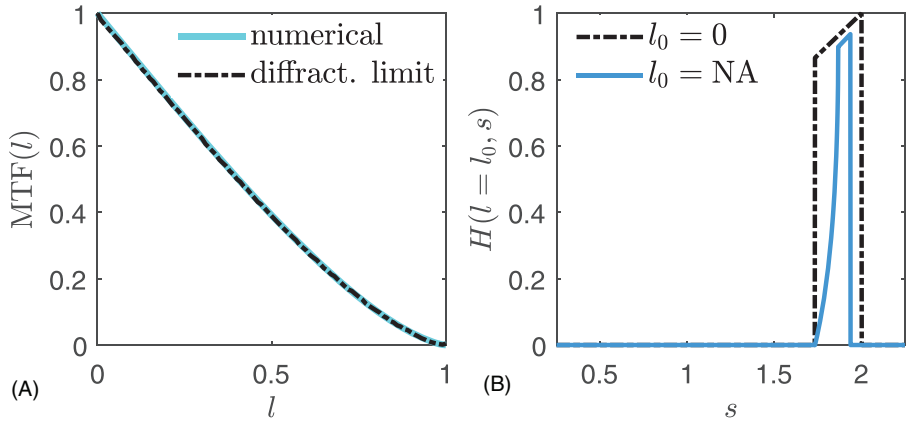

FIGURE 8 (A) Modulation transfer functions for a diffraction limited system of NA = 0.5 calculated by Equation (17) (indicated as 'diffract. limit') and obtained by numerical integration (indicated as 'numerical') of the 3D TF according to Figure 4 with respect to the s coordinate, (B) cross sections of the 3D TF according to Figure 4 for $l = l_0 = 0$ and $l = l_0 = \mathrm{NA}$

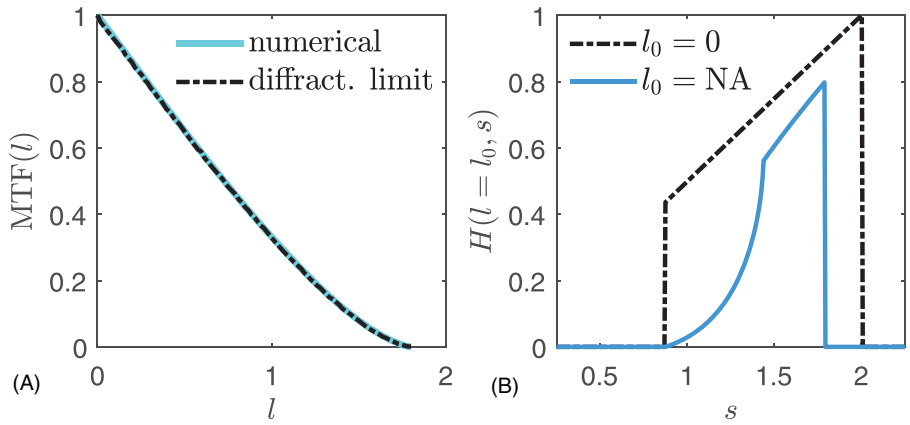

FIGURE 9 (A) Modulation transfer function for a diffraction limited system of NA = 0.9 calculated by Equation (17) (indicated as 'diffract. limit') and obtained by numerical integration (indicated as 'numerical') of the 3D TF according to Figure 5 with respect to the s coordinate, (B) cross sections of the 3D TF according to Figure 5 for $l = l_0 = 0$ and $l = l_0 = \mathrm{NA}$

(14) leads to negative contributions whereas the results of Equation (13) have a positive sign. The comparison of Figures 6 and 7 exhibits that with decreasing NA the contribution expressed by Equation (14) can be more and more neglected.

The integration of $H(l, s)$ according to Equation (16) with respect to the s-coordinate leads to the MTF:

$$\mathrm{MTF}(l) = \frac{2}{\pi}\left(\arccos\left(\frac{l}{2\,\mathrm{NA}}\right) - \frac{l}{2\,\mathrm{NA}}\sqrt{1 - \frac{l^2}{4\,\mathrm{NA}^2}}\right)$$
$$\sim \int_{-\infty}^{+\infty} H(l, s)\,\mathrm{d}s = A_1'(l) + A_2'(l), \qquad (17)$$

where the expression in the upper line of Equation (17) is the well-known formula for the diffraction limited MTF.[4] Corresponding results are displayed in Figures 8(A) and 9(A) for numerical apertures of 0.5 and 0.9, respectively. The analytical results given by the lower line of Equation (17) are denoted as 'diffract. limit'. Results of numerical integration of Equation (16) with respect to the s coordinate marked by 'numerical' perfectly agree to those calculated by the analytical formula. Figures 8(B) and 9(B) depict cross sections of $H(l, s)$ for constant l-values $l = l_0$ and numerical apertures of 0.5 and 0.9, respectively. For the specular direction, that is $l = 0$, $H(l = 0, s)$ is proportional to the coordinate s. For $l = \mathrm{NA}$ (blue lines in Figures 8B and 9B) the curves are narrower and no longer described by a straight line.

The 3D TF $H(l, s)$ according to Equation (16) depends on the normalized coordinates l and s. Expressing the 3D TF by spatial frequency coordinates requires a multiplication by the wavenumber $k_0 = 2\pi/\lambda$:

$$q_l = k_0\, l, \qquad q_s = k_0\, s \qquad (18)$$

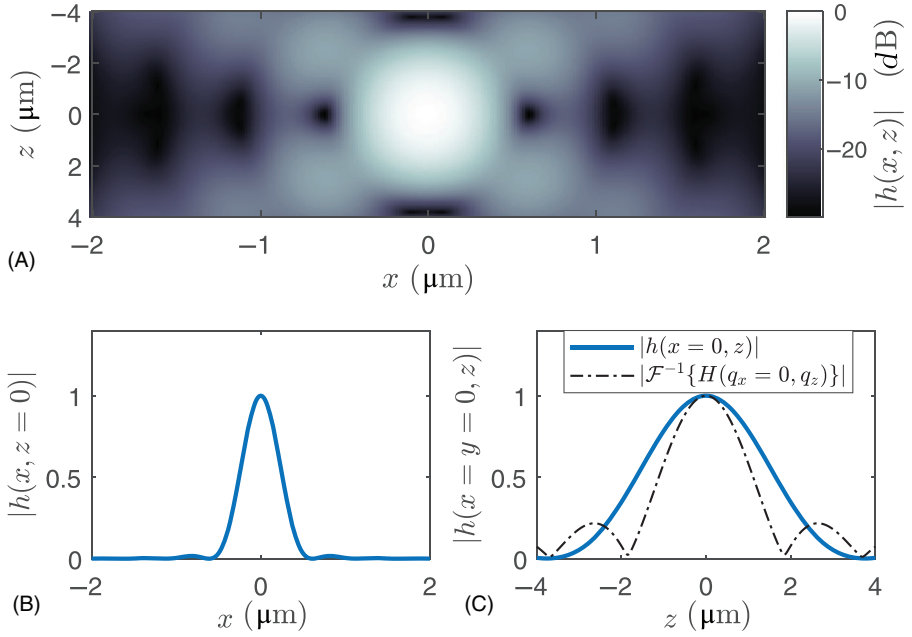

FIGURE 10 Intensity 3D-PSF for NA = 0.5 and $\lambda = 2\pi/k_0 = 0.5\ \mu$ m: (A) cross section in the xz-plane, (B) as a function of the transverse coordinate x assuming $y = z = 0$, (C) as a function of the axial coordinate z assuming $x = y = 0$

and thus leads to $H(\mathbf{q}, k_0)$ with $\mathbf{q} = (q_l, q_s)$. With this notation, the spatial frequency coordinates are directly related to the angular coordinates known from Kirchhoff scattering theory.[8,20,27]

The benefit of the 3D TF compared to the 2D MTF becomes obvious if $H(\mathbf{q}, k_0)$ is Fourier transformed with respect to all three spatial frequency coordinates, resulting in the 3D PSF $h(x, y, z)$. Due to the rotational symmetry, the transverse coordinates x and y can be substituted by the single coordinate $r = \sqrt{x^2 + y^2}$, representing the radial distance. Hence, $h(r, z)$ equals

$$h(r,z) = \frac{\int_0^\infty \mathrm{e}^{\mathrm{i}\, q_s z} \int_0^\infty H(q_l, q_s) J_0(q_l\, r)\, q_l\, dq_l\, dq_s}{\int_0^\infty \int_0^\infty H(q_l, q_s)\, q_l\, dq_l\, dq_s}, \qquad (19)$$

where J_0 represents the zero order Bessel function of the first kind and $h(r, z)$ is normalized such that the maximum value results in $h(r = 0, z = 0) = 1$. Examples of absolute values of this 3D PSF called intensity PSF are displayed in Figures 10 and 11 for NA = 0.5 and NA = 0.9, respectively. Figures 10(A) and 11(A) are colour-coded plots of cross sections of the $|h(x, y = 0, z)|$. Note that due to energy conservation,[16]) the total integrated intensity of $|h(x, y, z = \text{const.})|$ is constant along the z-axis. Therefore, a spatially resolving detector such as a camera is needed in the image plane (xy-plane) in order to locate the axial position of the point scatterer in a depth scanning process. The 2D PSFs according to Figures 10(B) and 11(B) result from the corresponding 3D PSFs for $z = 0$. Of course these curves equal the well-known Airy disc function, which results from the 2D Fourier transform of the 2D MTF.

Note that the total integrated intensity of a perfect mirror in a conventional bright-field microscope equals

$$I(z) = \int_0^\infty |H(q_l = 0, q_s)|\, dq_s \sim \int_0^\infty |h(r, z)|\, r\, dr. \qquad (20)$$

In contrast to Equation (19), where the phase information is considered due to the Fourier transform, Equation (20) integrates the intensity values on the spatial frequency axis q_s. Thus, the phase information is lost and an axial focus shift Δz will result in a phase shift of $H(q_l, q_s)$, which does not affect $I(z)$. Consequently, depth sectioning of mirror-like surfaces is not possible with a conventional microscope.[16]

Figures 10(C) and 11(C) represent the axial dependence of the 3D PSFs assuming $x = y = 0$. For comparison, Figures 10(C) and 11(C) additionally show the 1D axial PSFs, which result as the absolute value of the inverse Fourier transform of the intensity distribution along the q_s-axis $|\mathcal{F}^{-1}\{H(q_l = 0, q_s)\}|$.

Figures 10(C) and 11(C) reveal that $|h(x = 0, y = 0, z)|$ equals a sinc^2-function in the paraxial approximation, that is for low NA values as introduced by Wilson.[16] In contrast, for the nearly constant axial intensity distribution $H(q_l = 0, q_s)$ of the 3D TF according to Figure 4(C) the z-dependent intensity distribution follows a |sinc|-function

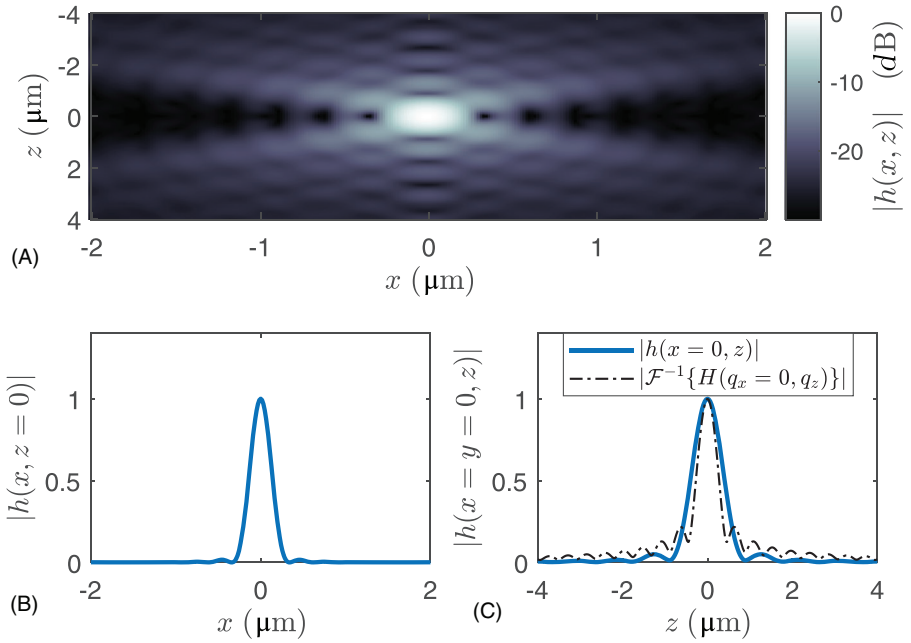

FIGURE 11 Intensity 3D-PSF for NA = 0.9 and $\lambda = 2\pi/k_0 = 0.5\ \mu$ m: (A) cross section in the xz-plane, (B) as a function of the transverse coordinate x assuming $y = z = 0$, (C) as a function of the axial coordinate z assuming $x = y = 0$

of half the width. In Figure 5(C), the axial intensity distribution $H(q_l = 0, q_s)$ of the 3D TF shows a ramp shape and thus, the corresponding absolute value of the Fourier transform in Figure 11(C) differs from an exact |sinc|-function. However, in general the axial 3D intensity PSF $|h(x = y = 0, z)|$ is broadened compared to $|\mathcal{F}^{-1}\{H(q_l = 0, q_s)\}|$, since for the computation of $h(x = y = 0, z)$ the integration runs over the whole 3D TF and the axial extension of $H(q_l \neq 0, q_s)$ is generally smaller than the axial extension of $H(q_l = 0, q_s)$. It should be noted, however, that due to the absolute value, the 3D intensity PSF $|h(x, y, z)|$ suffers from the loss of phase information. In Figure 12, the real part of $h(x, y, z)$ corresponding to the 3D PSF of the interference component in an interference microscope is displayed. Here, the high axial spatial frequency information can be observed as interference fringes Su et al.[14] and the NA-effect appears in a wider fringe spacing for higher NA.[5]

However, care must be taken, since the spatial frequency coordinates q_l and q_s are not independent of each other. For example, if the object under investigation is a flat mirror-like surface of uniform reflectance, the intensity in the spatial frequency domain will be concentrated on the q_s axis, that is there will be zero intensity for $q_l \neq 0$. Hence, the axial intensity distribution in the spatial domain equals the |sinc|-like 1D PSFs according to Figures 10(C) and 11(C) and no longer corresponds to $h(x = y = 0, z)$. Note that for a point scatterer under the paraxial approximation the 3D PSF of a CM in the axial direction is introduced as the square of the sinc^2-shaped axial PSF of a conventional

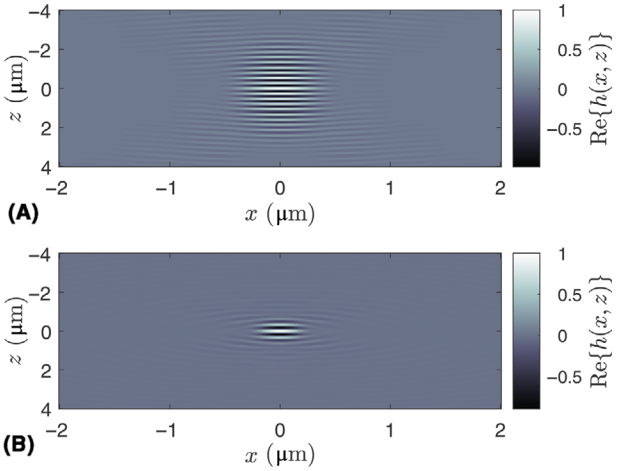

FIGURE 12 Cross sections in the xz-plane of the real part of the 3D PSF for $\lambda = 0.5\ \mu$ m and (A) NA = 0.5, (B) NA = 0.9

microscope and the square of the transverse PSF, that is the Airy disc function, in the image plane.[16]

Finally, the results of monochromatic illumination shown here can be easily extended to the case of broadband illumination if the spectral distribution of the light source $S_1(k_0)$ and the spectral sensitivity $S_2(k_0)$ of the system are considered for the calculation of the 3D TF by:

$$H(\mathbf{q}) = \int_0^\infty S_1(k_0)\, S_2(k_0)\, H(\mathbf{q}, k_0)\, dk_0. \tag{21}$$

4 | CONCLUSION

As shown in the previous sections, the 3D TF of diffraction limited microscopic imaging in reflection mode can be obtained through the correlation of two spherical caps, which are inverted to each other with respect to the optical axis. A given lateral shift of the spherical caps corresponds to a certain lateral spatial frequency. Hence, the integration along the optical axis of the overlapping surface sections of these caps projected into the lateral spatial frequency plane results in a cross-sectional area. This area equals the cross-sectional area of two circular functions of radius NA laterally shifted by the same amount as the spherical caps. Thus, the 3D TF derived by this method is in agreement with the well-known MTF of a diffraction limited incoherent microscopic imaging system under the assumption that the microscope is operated in reflection mode. The diffraction limited MTF represents something like the gold standard of incoherent optical imaging. However, the 3D TF introduced above represents a generalization of the MTF with respect to the axial intensity distribution. Thus, it becomes relevant if focus scanning systems or out-of-focus intensities of point scatterers are examined. Furthermore, the 3D TF of an incoherently illuminated microscope in reflection mode builds the basis for a comprehensive analysis of the imaging and measurement capabilities of instruments based on microscopic imaging. The inverse 3D Fourier transform of a 3D TF equals a 3D PSF. In the 3D point spread function of a CM, the out-of-focus intensities are blocked and the absolute values of the remaining 3D PSF are squared compared to those of a conventional microscope. This leads to a depth discrimination even for mirror-like surfaces and a better lateral resolution. With respect to 3D interference microscopy, for example CSI, the knowledge of the axial transfer characteristics at certain lateral spatial frequencies provided by the 3D TF is crucial for proper analysis and reconstruction of the object's surface and for appropriate setting of the parameters of signal processing algorithms.

ACKNOWLEDGEMENTS

Open access funding enabled and organized by Projekt DEAL.

ORCID

Peter Lehmann https://orcid.org/0000-0003-0051-5066

REFERENCES

1. Abbe, E. (1873). Beitrage zur Theorie des Mikroskops und der mikroskopischen Wahrnehmung. *Archiv für Mikroskopische Anatomie*, *9*, 413–468.
2. Lord Rayleigh, F. R. S. (1879). XXXI. Investigations in optics, with special referenceto the spectroscope. *Philosophical Magazine and Journal of Science, 5*, *8*(49), 261–274.
3. Hopkins, H. H. (1953). On the diffraction theory of optical images. *Proceedings of the Royal Society of London Series A*, *217*(1130), 408–432.
4. Goodman, J. W. (2005). *Introduction to Fourier optics*. Roberts and Company Publishers.
5. Sheppard, C., & Larkin, K. (1995). Effect of numerical aperture on interference fringe spacing. *Applied Optics*, *34*(22), 4731–4734.
6. McCutchen, C. W. (1964). Generalized aperture and the three-dimensional diffraction image. *Journal of the Optical Society of America*, *54*(2), 240–244.
7. Born, M., & Wolf, E. (2013). *Principles of optics: Electromagnetic theory of propagation, interference and diffraction of light*. Elsevier.
8. Sheppard, C. (1998). Imaging of random surfaces and inverse scattering in the Kirchoff approximation. *Waves in Random Media*, *8*(1), 53–66.
9. Quartel, J. C., & Sheppard, C. J. R. (1996). Surface reconstruction using an algorithm based on confocal imaging. *Journal of Modern Optics*, *43*(3), 469–486.
10. Gu, M. (2000). *Advanced optical imaging theory*. Springer.
11. Sarmis, M., Simon, B., Debailleul, M., Colicchio, B., Georges, V., Delaunay, J.-J., & Haeberle, O. (2010). High resolution reflection tomographic diffractive microscopy. *Journal of Modern Optics*, *57*(9), 740–745.
12. Sheppard, C., Gu, M., Kawata, Y., & Kawata, S. (1994). Three-dimensional transfer functions for high-aperture systems. *Journal of the Optical Society of America A*, *11*(2), 593–598.
13. Gross, H. (Ed.). (2005). *Handbook of optical systems*, *Vol. 2*, *Physical Image Formation (W. Singer, M. Totzeck, H. Gross)*. Wiley-VCH.
14. Su, R., Coupland, J., Sheppard, C., & Leach, R. (2021). Scattering and three-dimensional imaging in surface topography measuring interference microscopy. *Journal of the Optical Society of America A*, *38*(2), A27–A41.
15. Garces, D. H., Rhodes, W. T., & Pena, N. M. (2011). Projection-slice theorem: A compact notation. *Journal of the Optical Society of America A*, *28*(5), 766–769.
16. Wilson, T. (Ed.). (1990). *Confocal microscopy*. Academic Press, Inc.
17. Sheppard, C., Guo, M., & Mao, X. Q. (1991). Three-dimensional coherent transfer function in a reflection-mode confocal scanning microscope. *Optics Communications*, *81*(5), 281–284.
18. Sheppard, C., Connolly, T., & Gu, M. (1993). Imaging and reconstruction for rough surface scattering in the Kirchhoff approximation by confocal microscopy. *Journal of Modern Optics*, *40*(12), 2407–2421.
19. Nikolaev, N., Petzing, J., & Coupland, J. (2016). Focus variation microscope: Linear theory and surface tilt sensitivity. *Applied Optics*, *55*(13), 3555–3565.
20. Lehmann, P., Kunne, M., & Pahl, T. (2021). Analysis of interference microscopy in the spatial frequency domain. *IOP Journal of Physics: Photonics*, *3*, 014006.
21. Mandal, R., Coupland, J., Leach, R., & Mansfield, D. (2014). Coherence scanning interferometry: Measurement and correction of three-dimensional transfer and point-spread characteristics. *Applied Optics*, *53*(8), 1554–1563.

22. Su, R., Wang, Y., Coupland, J., & Leach, R. (2017). On tilt and curvature dependent errors and the calibration of coherence scanning interferometry. *Optics Express*, *25*(4), 3297–3310.
23. Su, R., Thomas, M., Leach, R., & Coupland, J. (2018). Effects of defocus on the transfer function of coherence scanning interferometry. *Optics Letters*, *43*(1), 82–85.
24. Su, R., Thomas, M., Liu, M., Drs, J., Bellouard, Y., Pruss, C., Coupland, J., & Leach, R. (2020). Lens aberration compensation in interference microscopy. *Optics and Lasers in Engineering*, *128*, 106015.
25. Lehmann, P., Xie, W., Allendorf, B., & Tereschenko, S. (2018). Coherence scanning and phase imaging optical interference microscopy at the lateral resolution limit. *Optics Express*, *26*(6), 7376–7389.
26. Lehmann, P., Tereschenko, S., Allendorf, B., Hagemeier, S., & Hüser, L. (2019). Spectral composition of low-coherence interferograms at high numerical apertures. *Journal of the European Optical Society-Rapid Publications*, 15(1), Article No. 5:1–9.
27. Beckmann, P., & Spizzichino, A. (1987). *The scattering of electromagnetic waves from rough surfaces*. Artech House, Inc.

How to cite this article: Lehmann P, Pahl T. Three-dimensional transfer function of optical microscopes in reflection mode. *Journal of Microscopy*. 2021:*284:*, 45–55.
https://doi.org/10.1111/jmi.13040